Received: 20 June 2016 | Revised: 31 October 2016 | Accepted: 28 December 2016

DOI: 10.1002/cnm.2863

WILEY

RESEARCH ARTICLE

High-resolution data assimilation of cardiac mechanics applied to a dyssynchronous ventricle

Gabriel Balaban[1,2,5] | **Henrik Finsberg**[1,2,5] | **Hans Henrik Odland**[4,7] | **Marie E. Rognes**[1,3] | **Stian Ross**[4,5] | **Joakim Sundnes**[1,2,5] | **Samuel Wall**[1,5,6]

[1]Simula Research Laboratory, P.O. Box 134 1325 Lysaker Norway
[2]Department of Informatics, University of Oslo, P.O. Box 1080, Blindern 0316 Oslo Norway
[3]Department of Mathematics, University of Oslo, P.O Box 1053, Blindern 0316 Oslo Norway
[4]Faculty of Medicine, University of Oslo, P.O. Box 1078 Blindern, 0316 Oslo Norway
[5]Center for Cardiological Innovation, Songsvannsveien 9, 0372 Oslo Norway
[6]Department of Mathematical Science and Technology, Norwegian University of Life Sciences, Universitetstunet 3 1430 Ås Norway
[7]Department of Pediatrics, Oslo University Hospital, PO Nydalen Oslo, Norway

Correspondence
Gabriel Balaban, Simula Research Laboratory, P.O. Box 134 1325 Lysaker, Norway.
Email: gabrib@math.uio.no

Funding information
Research Council of Norway; Center for Biomedical Computing at Simula Research Laboratory , Grant/Award Number: 179578; Center for Cardiological Innovation at Oslo University Hospital , Grant/Award Number: 203489

Abstract

Computational models of cardiac mechanics, personalized to a patient, offer access to mechanical information above and beyond direct medical imaging. Additionally, such models can be used to optimize and plan therapies in-silico, thereby reducing risks and improving patient outcome. Model personalization has traditionally been achieved by data assimilation, which is the tuning or optimization of model parameters to match patient observations. Current data assimilation procedures for cardiac mechanics are limited in their ability to efficiently handle high-dimensional parameters. This restricts parameter spatial resolution, and thereby the ability of a personalized model to account for heterogeneities that are often present in a diseased or injured heart. In this paper, we address this limitation by proposing an adjoint gradient–based data assimilation method that can efficiently handle high-dimensional parameters. We test this procedure on a synthetic data set and provide a clinical example with a dyssynchronous left ventricle with highly irregular motion. Our results show that the method efficiently handles a high-dimensional optimization parameter and produces an excellent agreement for personalized models to both synthetic and clinical data.

KEYWORDS

adjoint, cardiac mechanics, data assimilation, dyssynchrony, patient specific

1 | INTRODUCTION

Computational models of cardiac mechanics, personalized to the level of the individual through the use of clinical imaging, have potential to be a powerful aid in the diagnosis and treatment of cardiac disease. By relating image-based data to fundamental physical processes, models can give additional insight into the function or dysfunction of the individual's heart, beyond what can be directly measured or observed in the images. This is becoming more important as the resolution and accuracy of clinical imaging continues to improve. This increasingly detailed data combined with biophysical models have promise in analysis of regionally and temporally resolved differences in the mechanics of the heart, important in diseases such as heart failure and the application of cardiac resynchronization therapy.

A key step in making these clinically useful cardiac mechanics models is proper data assimilation from patient observations into a fit model. This involves the optimization, or tuning, of individual model parameters to make the model match the observations of the patient's heart. Over the last decade several data assimilation methods have been developed and proposed for this problem. The earliest studies used gradient-based optimization to minimize the discrepancy between model-derived data and clinical observations. The gradients necessary for these optimizations were calculated using direct differentiation[1] or finite difference.[2–4] More recent efforts include the use of global optimization methods: in particular, genetic algorithms,[5,6] a Monte Carlo method,[7] subplex algorithm,[8] and parameter sweeps.[9,10] Finally, reduced order unscented Kalman filtering has also been successfully applied as a data assimilation tool for patient-specific model creation.[11–13]

The increasingly large amount of easily obtainable geometric and motion data, however, is a challenge for data assimilation into personalized computational models using the techniques mentioned above. This is as the computational expense scales badly with the number of model parameters to be fit. In the case of the Kalman filtering strategies, at least 1 extra evaluation of the model is required per additional model parameter to be optimized. The calculation of model-data mismatch gradients by finite difference or direct differentiation suffers from the same limitation. Global methods on the other hand are affected by the curse of dimensionality, that is, a rapid expansion of the space of parameters that must be searched as the number of dimensions increases. For high-dimensional problems, the run time needed to conduct a global search can be computationally prohibitive.

In contrast, the calculation of a functional gradient by the adjoint formula is nearly independent of the number of optimization parameters, requiring 1 forward and 1 backward adjoint solve of the mathematical model. The forward solve is typically needed to evaluate the functional, and the evaluation of the gradient at the same point requires only an additional backward solve of the adjoint system. Furthermore, this backward solve is always linear and, therefore, computationally less expensive than the forward solve if the mathematical model is nonlinear. These methods have been widely explored in model optimization, with adjoint-based data assimilation techniques having previously been used for cardiac mechanics, specifically using linear elastic models and clinical data,[14,15] and also nonlinears model combined with experimental data.[16]

In this work, we provide an improved data assimilation pipeline for high-resolution optimization, demonstrating the parameterization of mechanical contraction in high spatial resolution driven by 4D echocardiography patient data. This high-dimensional optimization problem is efficiently solved using an adjoint gradient–based technique, described in detail in our previous work.[16] We demonstrate our method on the pathological case of a dyssynchronous left ventricle (LV), which has complex and irregular motion, as well as on a synthetic case consisting of data generated by our mechanical model. This study is to the best of our knowledge, the first to use adjoint-based data assimilation for nonlinear cardiac mechanics with clinical data, and the first to consider the resolution of a parameter at the same scale as the discretization of the cardiac geometry. These are important considerations as better understanding of myocardial properties emerges and the collection of high-resolution clinical data continues to expand.

The rest of this paper is organized as follows: In Section 2, we present a mathematical model that accounts for the 3 main drivers of ventricular mechanics: blood pressure, tissue elasticity, and muscle contraction. We also describe clinical measurements of a patient suffering from dyssynchrony and our data assimilation procedure for fitting the model to these measurements. Numerical results are presented in Section 3 and discussed in Section 4. Finally, we provide some concluding remarks in Section 5.

2 | MATERIALS AND METHODS

2.1 | Wall motion modelling

To estimate the position of the myocardial walls through the cardiac cycle, we adopt a continuum mechanics description of cardiac wall motion. In this description, we consider a fixed left ventricular (LV) reference geometry Ω, with endocardial boundary $\partial\Omega_{\text{endo}}$ and basal boundary $\partial\Omega_{\text{base}}$.

Our fundamental quantity of interest is the vector-valued displacement map $\mathbf{u}(\mathbf{X})$, where $\mathbf{X} \in \Omega$. At any given point in time in the cardiac cycle, $\mathbf{u}(\mathbf{X})$ relates the current geometry ω to the reference geometry by

$$\mathbf{X} + \mathbf{u}(\mathbf{X}) = \mathbf{x}, \quad \mathbf{x} \in \omega, \quad \mathbf{X} \in \Omega. \tag{1}$$

Assuming that the cardiac walls are in equilibrium, it is possible to determine the value of $\mathbf{u}$ from the principle of virtual work

$$\delta W(\mathbf{u}) = 0, \tag{2}$$

which states that the virtual work, $\delta W(\mathbf{u})$, of all forces applied to a mechanical system vanishes in equilibrium. For our ventricular wall motion model, the virtual work $\delta W(\mathbf{u})$, is given by

$$\begin{aligned} \delta W(\mathbf{u}, p) = &\int_\Omega \mathbf{P} : \text{Grad} \quad \delta\mathbf{u} \quad dV + \int_\Omega (J-1)\,\delta p \\ &+ pJ\mathbf{F}^{-T} : \text{Grad} \quad \delta\mathbf{u} \quad dV \\ &+ p_{\text{blood}} \int_{\partial\Omega_{\text{endo}}} J\mathbf{F}^{-T}\mathbf{N} \cdot \delta\mathbf{u} \quad dS \\ &+ \int_{\partial\Omega_{\text{base}}} k\mathbf{u} \cdot \delta\mathbf{u} \quad dS. \end{aligned} \tag{3}$$

Here, we have introduced the hydrostatic pressure p to enforce the incompressibility constraint $J = 1$, with $J = \det\mathbf{F} = \det(\text{Grad} \quad \mathbf{u} + \mathbf{I})$, and $\mathbf{I}$ being the second-order identity tensor. Furthermore, $\mathbf{N}$ denotes the unit outward normal vector, k the constant of a spring that we introduce at the basal boundary, and p_{blood} the intraventricular blood pressure. The virtual variables $\delta\mathbf{u}$ and δp are test functions whose values are arbitrary when the system (Equation 2) is in mechanical equilibrium.

To anchor the computational geometry, we fix $\mathbf{u}$ in the longitudinal direction at the base by using a Dirichlet boundary condition. At the epicardial boundary, normal forces are set to 0, and so there is no term for this boundary in Equation 3.

The internal stresses of our model are given by $\mathbf{P}$, the first Piola-Kirchhoff tensor, which can be calculated as a derivative of a strain energy functional in the case of a hyperelastic material. In our model, we use a reduced version[9,10,17,18] of the Holzapfel-Ogden strain energy law,[19]

$$\psi(\mathbf{C}) = \frac{a}{2b}\left(e^{b(I_1(\mathbf{C})-3)} - 1\right) + \frac{a_f}{2b_f}\left(e^{b_f(I_{4f}(\mathbf{C})-1)_+^2} - 1\right), \quad (4)$$

which gives the amount of strain energy, ψ, stored per unit volume myocardium undergoing the deformation $\mathbf{C} = \mathbf{F}^T\mathbf{F}$. The notation $(\cdot)_+$ refers here to $\max\{\cdot, 0\}$. Furthermore, the mechanical invariants I_1 and I_{4f} are defined as

$$I_1(\mathbf{C}) = \text{tr}\,\mathbf{C}, \qquad I_{4f} = \mathbf{e_f} \cdot \mathbf{C}\mathbf{e_f}, \quad (5)$$

with $\mathbf{e_f}$ indicating the local myocardial fiber direction. The material parameters a, a_f, b, and b_f are scalar quantities, which influence the shape of the stress-strain relationship, and can be adapted to personalize the elastic properties of a myocardial tissue model to a specific patient.

The Lagrange multiplier formulation of incompressibility that we use enforces its constraint only weakly. This can cause convergence issues in the numerical solution of the work balance equation (Equation 2). We therefore eliminate volumetric strains from the energy function (Equation 4) by a simple modification

$$\tilde{\psi}(\mathbf{C}) = \psi\left(J^{-\frac{2}{3}}\mathbf{C}\right). \quad (6)$$

This modification has been shown to improve the robustness of Newton-Raphson methods applied to incompressible hyperelastic problems [Figure 3C[20]].

To account for muscle contraction, we apply the active strain framework.[21] In this framework, the amount of muscle fiber shortening is specified by a field γ via a split of the deformation gradient

$$\mathbf{F} = \mathbf{F}_e\mathbf{F}_a(\gamma), \quad (7)$$

where $\mathbf{F}_e$ is the elastic part and $\mathbf{F}_a(\gamma)$ is the active part of the deformation gradient. For the value of $\mathbf{F}_a(\gamma)$, we adopt a simple relation[18,22] that satisfies the incompressibility constraint by design and directly relates the amount of active fiber shortening to the value of γ

$$\mathbf{F}_a = (1-\gamma)\mathbf{e}_f \otimes \mathbf{e}_f + \frac{1}{\sqrt{1-\gamma}}(\mathbf{I} - \mathbf{e}_f \otimes \mathbf{e}_f). \quad (8)$$

In the case $\gamma = 0$, there is no muscle shortening at all, and the amount of shortening increases with increased γ up to the theoretical limit of $\gamma = 1$. Physiologically, γ models the length change along muscle fibers neglecting elastic effects. This, together with the elastic resistance gives the strength of the muscle contraction.

Muscle contraction is accounted for in terms of virtual work by modifying the first Piola-Kirchhoff stress tensor so that the strain energy only depends on the elastic part of the deformation

$$\mathbf{P} = \frac{\partial\tilde{\psi}}{\partial\mathbf{F}} = \frac{\partial\tilde{\psi}(\mathbf{C}_e)}{\partial\mathbf{F}} \quad (9)$$

with $\mathbf{C}_e = \mathbf{F}_e^T\mathbf{F}_e$.

Given an amount of fiber shortening γ, the value of the elastic parameters a, b, a_f, and b_f, the intraventricular blood pressure p_{blood} and the spring constant k, the myocardial wall displacement $\mathbf{u}$ and hydrostatic pressure p can be obtained by solving the principle of virtual work (Equation 2).

2.2 | Clinical measurements

Clinical data were obtained at the Oslo University Hospital in the context of the Impact study.[23] Specifically, we consider the case of an 82-year-old man in New York Heart Association functional class III systolic heart failure with coronary artery disease and left bundle branch block. A left bundle branch block normally causes both electrical and mechanical dyssynchrony. In this case, electrocardiography revealed a QRS width of 140 ms and the echocardiographically derived ejection fraction was 30 %.

Prior to cardiac resynchronization therapy implant, the patient had echocardiographic and LV pressure measurements taken, which are the basis for the clinical data used in this study. Pressure recordings were conducted with an intravascular pressure sensor catheter (Millar microcatheter) that was positioned in the LV via the right femoral artery. Pressure data were obtained automatically and digitized (Powerlab system, AD Instruments) before off-line analyses were performed with a low pass filter of 10 Hz.

Images of the patient's LV were captured with 4-D echocardiography using a GE Vingmed E9 machine (GE healthcare Vingmed, Horten, Norway). Speckle tracking motion analysis was conducted with GE's software package EchoPac. Data from 6 beats were combined in EchoPac to obtain a single sequence of images for a single heartbeat. Analysis of these images resulted in LV cavity volume measurements as well as regional strain curves defined for a 17 segment delineation of the LV according to the American heart association (AHA) representation.[24] The strain curves were measured in the local LV longitudinal, radial, and circumferential directions. Both strains and volumes were measured 34 times throughout the cardiac cycle.

Valvular events were used to synchronize the pressure to the strain and volume data. The timing of the observed valvular events in the images were matched with the observed valvular events in the pressure trace. In the pressure trace, aortic valve opening was selected after the steepest increase of the pressure ($\frac{dp}{dt}$ max) and mitral valve closure just before $\frac{dp}{dt}$ max . Aortic valve closure was chosen just before the pressure had its largest decrease after aortic valve opening, and the mitral valve opening before the pressure dropped down to baseline after aortic valve closure. A pressure-volume (PV) loop based on the synchronization is displayed in Figure 2.

Finally, a linear correction of the strain curves was performed to eliminate drift, with drift being defined as the value of the strain obtained at the end of the cardiac cycle. Theoretically, drift should be zero for a stable cyclical heartbeat. The linear correction enforces the cyclical property.

2.3 | Ventricular geometry generation

The computational mechanics framework used for our wall motion model, described in Section 2.1, requires a reference stress-free geometry from which to define displacements. Such a geometry typically does not exist in vivo due to the presence of blood pressure on the endocardial walls. Algorithms exist for calculating stress-free geometries given a loaded state.[25,26] However, for the sake of simplicity, we derive our reference geometry from an echocardiographic image of the LV at the beginning of atrial systole, as the pressure is near minimal at this point, and the ventricular myocardium can be assumed to be relaxed.

From the image at the beginning of atrial systole, triangulated data points for LV endocardial and epicardial surfaces, along with a 17 segment delineation, were extracted using the EchoPac software package. The segment delineation was given on a so called strain mesh, which is a 2-D surface constructed by EchoPac and located approximately in the mid wall of the LV.

We constructed a flat ventricular base by cutting the raw geometry with a plane that was fit via least squares to the points at the base. After the fitting, the longitudinal position of the cutting plane was adjusted so that the cavity volume of the resulting mesh agreed with the measured volume to a tolerance of 1 mL. Points on the epicardial and endocardial surfaces that lay above the cutting plane were removed.

We used Gmsh[27] to create a linear tetrahedral volumetric mesh between the endocardial and epicardial surfaces. This mesh had 1262 elements and is shown in Figure 1B. Myocardial fiber orientations were assigned using a rule-based method, with a fiber helix angle of 40° on the endocardium rotated clockwise throughout the ventricular wall to $-50°$ on the epicardium.[28] A streamline representation of the local myocardial fibers is displayed in Figure 1C.

Finally, the AHA segments from the strain mesh were transferred onto the volumetric mesh. This was accomplished by computing prolate spherical coordinates for the barycenter of each tetrahedron and then assigning an AHA zone to the tetrahedron based on the corresponding prolate spherical coordinate in the strain mesh. AHA segments on the volumetric mesh are shown in Figure 1D.

2.4 | Parameter estimation

Now that we have a mathematical description of cardiac motion, along with a personalized computational geometry and target data, we next turn to the problem of personalizing the motion model via the estimation of the elastic parameters and the fiber contraction. As dyssynchrony is a disease which primarily affects the contraction properties of the ventricle, we focus our efforts on contraction modelling and use a very simple personalization of stiffness properties. That is, only the parameter a is optimized to fit the ventricular volumes, and the other elastic parameters are kept fixed at the values ($a_f = 1.685$ kPa, $b = 9.726$, $b_f = 15.779$), which were obtained from a bi-axial loading experiment [Table 1 row 3[19]].

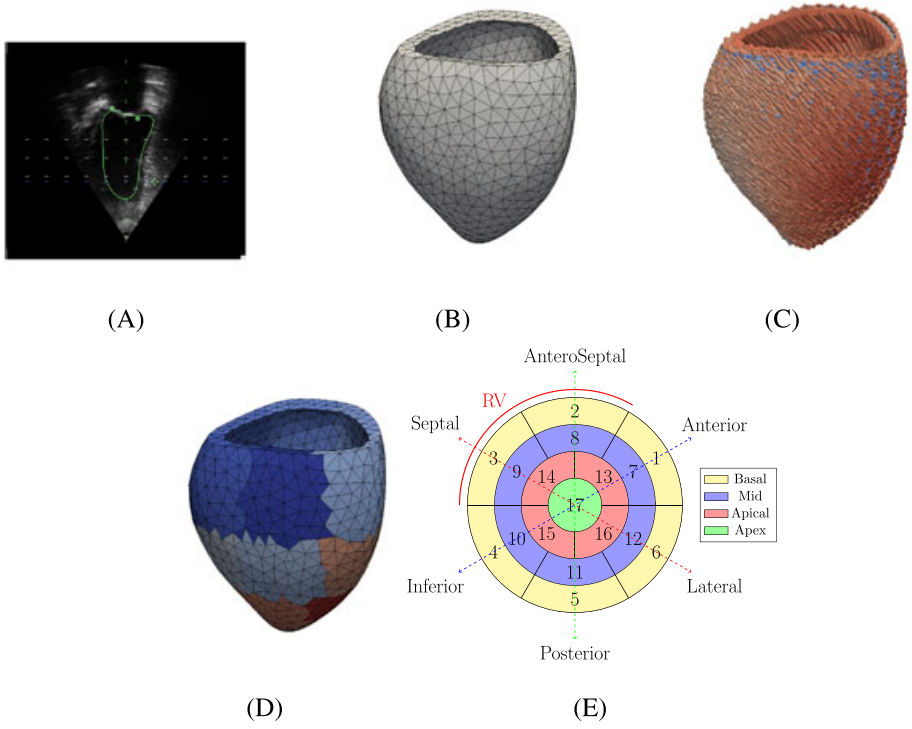

FIGURE 1 Ventricular geometry generation. Endocardial and epicardial surfaces are marked on 3-D ultrasound images. A, The endocardial marking for a 2-D slice of 1 such image. B, A computational geometry is generated from epicardial and endocardial surfaces. C, Rule-based fibers are assigned. D, AHA segments are assigned to the geometry, according to E, standardized scheme

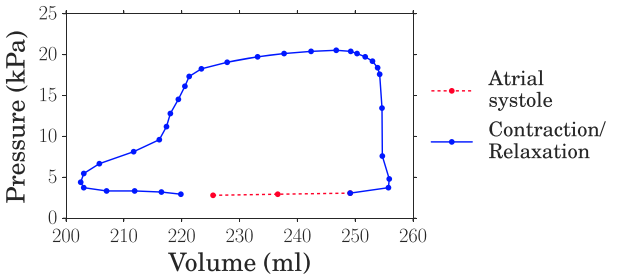

FIGURE 2 Patient pressure-volume relationship for the left ventricle. Measurements in the blue solid line are used to estimate contraction, whereas measurements in the red dashed line are used to estimate elasticity

Fiber contraction varies throughout the cardiac cycle, and so we estimate the parameter γ separately at each time measurements were taken. Furthermore, as the contraction of the LV may occur dyssynchronously, we allow for γ to vary in space as well as in time.

Muscle shortening is typically present in the ventricles throughout systole and in early diastole until the muscles fully release their contraction. During the phase of atrial systole, we do not expect muscle contraction in the ventricle, and so we set $\gamma = 0$ for this phase. This allows us to estimate elastic properties independently of contraction during atrial systole, and then estimate contraction at each point in the rest of the cardiac cycle with the material parameters fixed. In Figure 2, we show the pressure-volume loop of the patient under consideration and highlight the phases where we estimate the contraction and elastic parameters.

2.5 | Definition of functionals

As described in Section 2.2, the data available for our personalization of the wall motion model are pressure, volume, and strain measurements throughout the cardiac cycle. The pressure measurements are included in the model as a boundary condition via the virtual work (Equation 2), and thus our data assimilation only needs to fit the model to the volume and strain measurements. This requires that we define a suitable set of functionals that quantify the model-strain and model-volume mismatches. The personalization of the wall motion model can then be achieved by optimizing the contraction and elastic parameters to minimize the total model-data mismatch.

Let i denote the index of an observed cavity volume V^i, or strain ε^i, in the cardiac cycle. Furthermore, let $j \in \{1, .., 17\}$ be the index of an AHA segment Ω_j and $k \in \{c, r, l\}$ indicate a direction: circumferential, radial or longitudinal, respectively. Given a measurement point i, we define the model-strain mismatch

$$I^i_{\text{strain}} = \sum_{j=1}^{17} \sum_{k\in\{c,r,l\}} \left(\varepsilon^i_{kj} - \tilde{\varepsilon}^i_{kj}\right)^2, \tag{10}$$

for model strain $\tilde{\varepsilon}^i_{kj}$ and measured strain ε^i_{kj}. The speckle tracking software we use provides the measured strain ε^i_{kj}. This strain is regionally averaged and of Lagrangian type. To mimic this in our model, we define the model strain as

$$\tilde{\varepsilon}^i_{kj} = \frac{1}{|\Omega_j|}\int_{\Omega_j} \mathbf{e}_k^T \nabla \mathbf{u}\, \mathbf{e}_k \, dx, \tag{11}$$

where $\mathbf{e}_k$ denotes a unit direction field and $|\Omega_j|$ the volume of segment j.

Furthermore, we also define the model-volume mismatch

$$I^i_{\text{vol}} = \left(\frac{V^i - \tilde{V}^i}{V^i}\right)^2, \tag{12}$$

where the model volume is calculated by the formula

$$\tilde{V}^i = -\frac{1}{3}\int_{\partial\Omega_{\text{endo}}} (\mathbf{X} + \mathbf{u}) \cdot J\mathbf{F}^{-T}\mathbf{N} \quad dS. \tag{13}$$

We note that this method of calculating the model volume depends upon $(\mathbf{X} + \mathbf{u})\cdot\mathbf{N} = 0$ at the basal plane. These conditions hold in our model as the basal plane is defined with 0 longitudinal coordinate and longitudinal displacements are also set to 0 in this plane.

To have a single optimization target to describe the fit to data, we combine the strain (Equation 10) and volume (Equation 13) mismatches into 1 single functional

$$I^i_{\text{data}}(\alpha) = \alpha I^i_{\text{vol}} + (1-\alpha) I^i_{\text{strain}}. \tag{14}$$

Here, the parameter α controls the relative emphasis of the parameter estimation on volume or strain matching.

In our study, we consider a high-dimensional representation of γ to more accurately capture the details of a dyssynchronous contraction. However, this can easily lead to an over-parametrized problem in which many parameter combinations produce the same functional values. To further constrain the optimization, we introduce a first-order Tikohonov regularization functional

$$I^i_{\text{smooth}}(\lambda) = \lambda \|\nabla \gamma^i\|^2, \tag{15}$$

where $\|\cdot\|$ represents the standard L^2 norm. This functional discriminates between γ parameter sets based on their smoothness. The parameter λ can be adjusted to control the size of the functional and hence the relative emphasis on smoothing.

2.6 | Parameter estimation as an optimization problem

The elastic parameters of the reduced Holzapfel-Ogden law (Equation 4) represent the passive elastic properties of the myocardium. We personalize these properties by adjusting the parameter a to match measured LV volumes. Mathematically, this problem is formulated as

$$\begin{aligned} \underset{a}{\text{minimize}} \quad & \sum_{i=1}^{N_{\text{AS}}} I^i_{\text{vol}} \\ \text{subject to} \quad & \delta W\left(p^i_{\text{blood}}, a\right) = 0 \quad \forall\, i \quad \in \{1, ...N_{AS}\}, \end{aligned} \tag{16}$$

where δW is given by Equation 3 and $N_{\text{AS}} = 3$ indicates the total number of measurements available in atrial systole.

The contraction field that we seek should fit the data as closely as possible while also being as smooth as possible. To achieve this, we minimize both the data and smoothness functionals as follows:

$$\begin{aligned} \underset{\gamma}{\text{minimize}} \quad & I^i_{\text{data}}(\alpha) + I^i_{\text{smooth}}(\lambda) \\ \text{subject to} \quad & \delta W\left(p^i_{\text{blood}}, a, \gamma^i\right) = 0 \\ & \gamma^i(\mathbf{X}) \in [0, 1), \quad \mathbf{X} \in \Omega. \end{aligned} \tag{17}$$

This problem is solved for every measurement point i not in atrial systole.

The optimization problems (Equations 16 and 17) have 2 free parameters whose values must be chosen, namely, the strain-volume weighing α and the regularization λ. The value of λ can be expected to influence the trade-off between the optimized values of the data functional I^i_{data} and the regularization functional I^i_{smooth}. Similarly, α can be expected to influence the trade-off between I^i_{strain} and I^i_{vol}. In our study, we choose the values of α and λ by examining their effects on the functionals that they weigh. The choices we made are further described in Section 3.3

The spatial resolution of the parameter γ affects the amount of detail that can be captured by the model and simultaneously the number of variables that need to be optimized. We therefore test 3 different resolutions of γ. The lowest resolution, "scalar," is simply a single global value. The next resolution is "regional" and consists of a separate value for each of the 17 AHA zones. Finally, the highest resolution we consider is "P1" and consists of a separate value at each of the vertices of the mesh, with a linear interpolation between vertices. Using our ventricular mesh, a P1 resolution of γ has 1262 separate variables.

2.7 | Implementation of mechanics and optimization solvers

For the numerical solution of the work balance equation (Equation 2), we use a Galerkin finite element method with Taylor-Hood tetrahedral elements,[29] that is, a continuous piecewise quadratic representation of the displacement field and a continuous piecewise linear representation of the pressure field.

The software implementation of our finite element method is based on the package FEniCS,[30] which automatically generates matrix and vector assembly code from a symbolic representation of the work balance equation (Equation 2). The resulting nonlinear systems were solved using the PETSc implementation of a Newton trust region algorithm,[31] while the inner linear solves were handled by a distributed memory parallel LU solver.[32]

To solve the optimization problems (Equations 16 and 17), we apply a sequential quadratic programming (SQP) algorithm.[33] This algorithm requires the derivatives of the function to be optimized, which in our case are the gradients of the mismatch functionals in problems (Equations 16 and 17) with respect to a and γ, respectively. These gradients are automatically computed by solving a machine derived adjoint equation via the software framework dolfin-adjoint.[34]

In addition to gradients, the SQP algorithm requires evaluations of the mismatch functionals for given values of the control variables, which again relies on the solution of the work balance equation (Equation 2). In the case of the problem (Equation 17), the control variable is γ, which has a large influence on the solution of Equation 2. Numerical solution of Equation 2 by Newton method depends upon having a good initial guess, which in our case are the values of the mechanical state variables, $\mathbf{u}$, p, resulting from the previous solve of Equation 2. If the value of γ differs too greatly from one solve to the next, the Newton algorithm might fail due to the root of the system being too far away from the initial guess. To avoid this problem, we make use of a homotopy procedure that moves from one value of γ to the next in small increments and solves Equation 2 each time the value of γ is changed. This procedure is presented as Algorithm 1 and is similar to one that has been previously published.[35]

All algorithms, solvers, and relevant data are publicly available online.[36]

2.8 | Error estimation

The optimization functionals introduced in Section 2.5 are defined separately for each measurement point. For the purposes of evaluating goodness of fit over the entire cardiac cycle, we consider metrics that are averaged over measurement points. Furthermore, we relate errors to the sizes of the data for ease of interpretation. In the case of the model-volume error, we introduce the volume metric

$$\bar{I}_{\text{vol}} = \frac{\|V^i - \tilde{V}^i\|_{\ell^1}}{\|V^i\|_{\ell^1}}, \tag{18}$$

where the ℓ^1 norm is taken with respect to the measurement point index i. Furthermore, we consider 2 average strain metrics

$$\bar{I}_{\text{strain}} = \frac{1}{51}\sum_{j=1}^{17}\sum_{k\in\{c,r,l\}}\frac{\|\varepsilon^i_{k,j} - \tilde{\varepsilon}^i_{k,j}\|_{\ell^1}}{\|\varepsilon^i_{k,j}\|_{\ell^1}}, \tag{19}$$

$$\bar{I}^{\text{relmax}}_{\text{strain}} = \frac{1}{51}\sum_{k\in\{c,r,l\}}\frac{\sum_{j=1}^{17}\|\varepsilon^i_{k,j} - \tilde{\varepsilon}^i_{k,j}\|_{\ell^1}}{\max_j\|\varepsilon^i_{k,j}\|_{\ell^1}}. \tag{20}$$

Here, N specifies the number of measurement points used in the optimization, and the factor 51 is 17×3, the number of AHA segments times the number of strain measurements per segment. The first metric considers relative differences between norms, whereas the second relates errors norms to the maximum strain norm over all segments. This second metric emphasizes larger features in the strain curves more heavily and deemphasizes small scale features such as noise.

Similar to the average data errors introduced above, we also introduce a smoothness metric that is averaged across measurement points

$$\bar{I}_{\text{smooth}} = \frac{1}{N}\sum_{i=1}^{N} I^i_{\text{smooth}}, \tag{21}$$

and a combined data metric based on the strain and volume metrics

$$\bar{I}_{\text{data}} = \bar{I}_{\text{vol}} + \bar{I}_{\text{strain}}. \tag{22}$$

Finally, we also define an error metric for a synthetic data test of the contraction optimization (Equation 17). In this test, a contraction field γ_{ground} is chosen and synthetic data are generated from the mechanics model. These data are then used to calculate a reproduction of the contraction, γ_{repr}. In order to compare the ground truth and reproduced contraction fields, we use a relative L^2 norm

$$\|\varepsilon_\gamma\|_{\text{avg}} = \frac{1}{N}\sum_{i=1}^{N}\frac{\|\gamma^i_{\text{repr}} - \gamma^i_{\text{ground}}\|_{L^2}}{\|\gamma^i_{\text{ground}}\|_{L^2}}. \tag{23}$$

3 | NUMERICAL EXPERIMENTS

In this section, we present the results of our numerical experiments. We first estimate the parameter a using volume measurements in atrial systole. We then test the estimation of contraction γ using synthetic data generated by the wall motion model. This gives an idea of how well the algorithm can perform under idealized circumstances. Next, we conduct the contraction estimation using the clinical strain and volume data. Finally, we consider lower resolution representations of γ and compare the resolutions based on computational expense and data matching capability.

In all of the experiments below, optimizations were terminated if the difference between the value of the mismatch in the current and previous iteration was less than 10^{-9} for the passive material parameter optimization and 10^{-6} for the contraction parameter optimization or if the SQP algorithm was not able to further reduce the mismatch value. In the contraction optimization, the SQP algorithm was initialized with the value of γ from the previous measurement point in the cardiac cycle.

To obtain convergence of Newton method for the solution of the virtual work (Equation 2), we set $\delta\gamma_{max} = 0.02$ in the homotopy Newton solver (Algorithm 1) and limited γ to the interval [0, 0.9]. In the cases that Newton method did not converge, $\delta\gamma_{max}$ was halved until convergence was obtained.

Algorithm 1 Max Increment Homotopy Newton Solver

Initial Variables

$\mathbf{u}_{prev}$	Previous displacement field
p_{prev}	Previous tissue hydrostatic pressure field
γ_{next}	Desired tissue contraction field
$\delta\gamma_{max}$	Maximum change in a component per Newton solve

Set

$\gamma_0 = \gamma_{prev}$
$\mathbf{u}_0 = \mathbf{u}_{prev}$
$p_0 = p_{prev}$
$M = \left\lceil \frac{\|\gamma_{next} - \gamma_{prev}\|_\infty}{\delta\gamma_{max}} \right\rceil$
$\delta\gamma = \frac{1}{M}(\gamma_{next} - \gamma_{prev})$

Use Newton's method M times with fixed increment $\delta\gamma$
for $i \in \{1...M\}$ **do**
  $\gamma_i = \gamma_{i-1} + \delta\gamma$
  Initialize Newton solver with $\mathbf{u}_{i-1}, p_{i-1}$
  Solve $\delta W(\mathbf{u}_i, p_i, \gamma_i) = 0$ for $\mathbf{u}_i, p_i$
Output $\mathbf{u}_i, p_i$

Strains were calculated with respect to the measurement point defined as start of atrial systole, as the reference geometry taken from the image corresponding to this point was assumed to be stress and strain free. Similarly, pressures for the clinical data were adjusted downward by the pressure measured at the start of atrial systole, 2.8 kPa, so that the adjusted start of atrial systole pressure was 0, and therefore compatible with the stress free assumption.

The value of the basal spring constant was set to $k = 1.0$ kPa. This allowed for some motion in the basal plane and was shown in a sensitivity analysis (see Appendix B) to give optimal γ values whose spatial average is close to that obtained with a completely fixed boundary.

3.1 | Estimation of elastic parameter a

An estimate of the parameter a was obtained by minimizing the mismatch between model-derived and clinically measured volumes in atrial systole, as described in Equation 16. The optimal a value obtained was 0.435, with goodness of fit $\bar{I}_{\text{vol}} = 0.0035$. The same optimal a value was also obtained from 8 randomly chosen starting points between 0 and 45.

3.2 | Synthetic dataset creation

To evaluate the performance of our contraction estimation method (Equation 17) under idealized conditions, we have performed synthetic data tests. The data for these tests was constructed by solving the virtual work (Equation 2) for a given set of elastic parameters (a, a_f, b, and b_f), contraction γ, and cavity pressures. The a parameter was set to 0.435 kPa, as obtained previously by fitting the model to the patient atrial systolic volume data. The other 3 elastic parameters were fixed to the values mentioned in Section 2.4. The contraction γ was chosen to be a wave with Gaussian shape and P1 resolution traveling along the longitudinal axis.

Eight points of measurement were used in the synthetic tests. This was fewer than the number of in vivo measurement points, which allowed for faster computations. The pressure values that were chosen for the synthetic measurement points can be seen in Figure 5. These pressures start at 0, increase to the maximum atrial systole pressure that was measured in vivo and then decrease linearly back to 0.

For the synthetic strain data, we considered 3 different cases. The first case consisted of the displacement gradient tensor defined over the entire ventricular geometry. Next, we considered regionally averaged values of the diagonal components of the displacement gradient. The regional averaging mimics the strain curves generated by the speckle tracking software. Finally, we consider 30 noisy realizations of the regional strain curves. The noise that was added to these curves was estimated from the drift values of the in vivo strain and is described in Appendix E.

3.3 | Choice of functional weights α and λ

The optimization functional weights α and λ were chosen based on trial optimizations using the synthetic and in vivo datasets. The strains in the synthetic data were regionally averaged and noisy. In these trials, we first set $\lambda = 0$ and tested α values ranging from 0 to 1.0 in increments of 0.1, in addition to the values 0.95, 0.99, 0.999, and 0.9999. For each level of α, we recorded the values of the fit metrics, $\bar{I}_{\text{vol}}$ and $\bar{I}_{\text{strain}}$, and plotted them against each other (Figure 3). On the basis of the plot, we chose $\alpha = 0.95$ as this value gave a good balance between volume and strain matching. With the value of α fixed to 0.95, we tested λ from 10^{-6} to 100.0 in increasing powers of 10. The effect of the choice of λ on the smoothness and data functionals is shown in Figure 3. On the basis of this plot, we selected points that gave near optimal fit values with a high level of smoothness. These points were $\lambda = 1.0$ for the synthetic case and $\lambda = 0.01$ for the patient case.

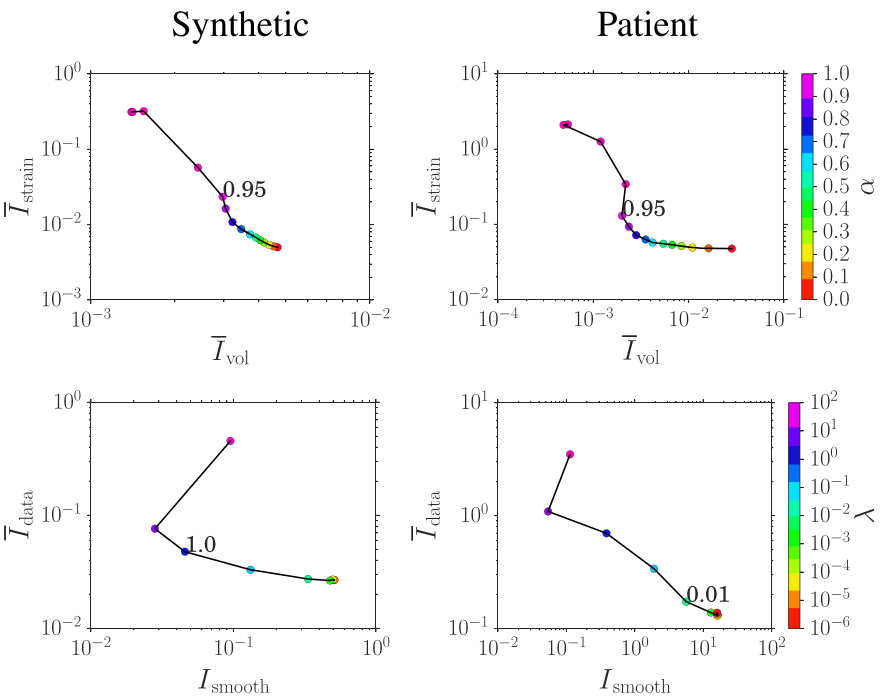

FIGURE 3 Trade-off curves for various α and λ values used in model personalization with synthetic strain data and in vivo patient data. The synthetic strains are noisy and regionally averaged. The contraction parameter is represented at P1 resolution. Top: optimal strain mismatch (Equation 20) versus average volume mismatch (Equation 18) for a range of α values and $\lambda = 0.0$. Bottom: Total data mismatch versus contraction gradient size for a range of λ values and $\alpha = 0.95$

3.4 | Contraction estimation with synthetic data

Using the synthetic datasets described in Section 3.2 as a target, we calculated optimized contraction fields. All elastic parameters were kept fixed throughout the optimization so that the test was restricted to the contraction field. We quantified the error in the reproduction of γ using P1 resolution for the 3 cases of strain. Errors in the relative norm, $\|\epsilon_\gamma\|_{\text{avg}}$, were 0.033 for the full displacement gradient tensor and 0.227 for the regionally averaged diagonal of the displacement gradient without noise. The average error for the 30 noisy regionally averaged cases was 0.224 with a standard deviation of 0.009. We note that the reproduction error was lowest for the full clean strains, and an order of magnitude higher for the regional clean and regional noisy strains. We also note that the reproduction error using regional clean strains was very close to the average reproduction error from the 30 regional noisy strains. The maximum error for all 3 cases of strain occured in the apex and was 0.06, 0.0701, 0.0724 for the full, regional clean, and regional noisy cases, respectively.

For the case of the full clean strains, we have plotted the reconstructed contraction field alongside the ground truth in Figure 4. We note that the ground truth and reproduction appear very similar. To visualize the effect of the noise in strain on the optimized contraction field, we plotted the mean and standard deviation of the 30 synthetic strain curves and mean and standard deviation of the average of the contraction field resulting from the 30 strain curves. Both of these plots are restricted to the anterior basal segment and are shown in Figure 5. We note that the effect of the noise on the optimized average contraction field is minimal.

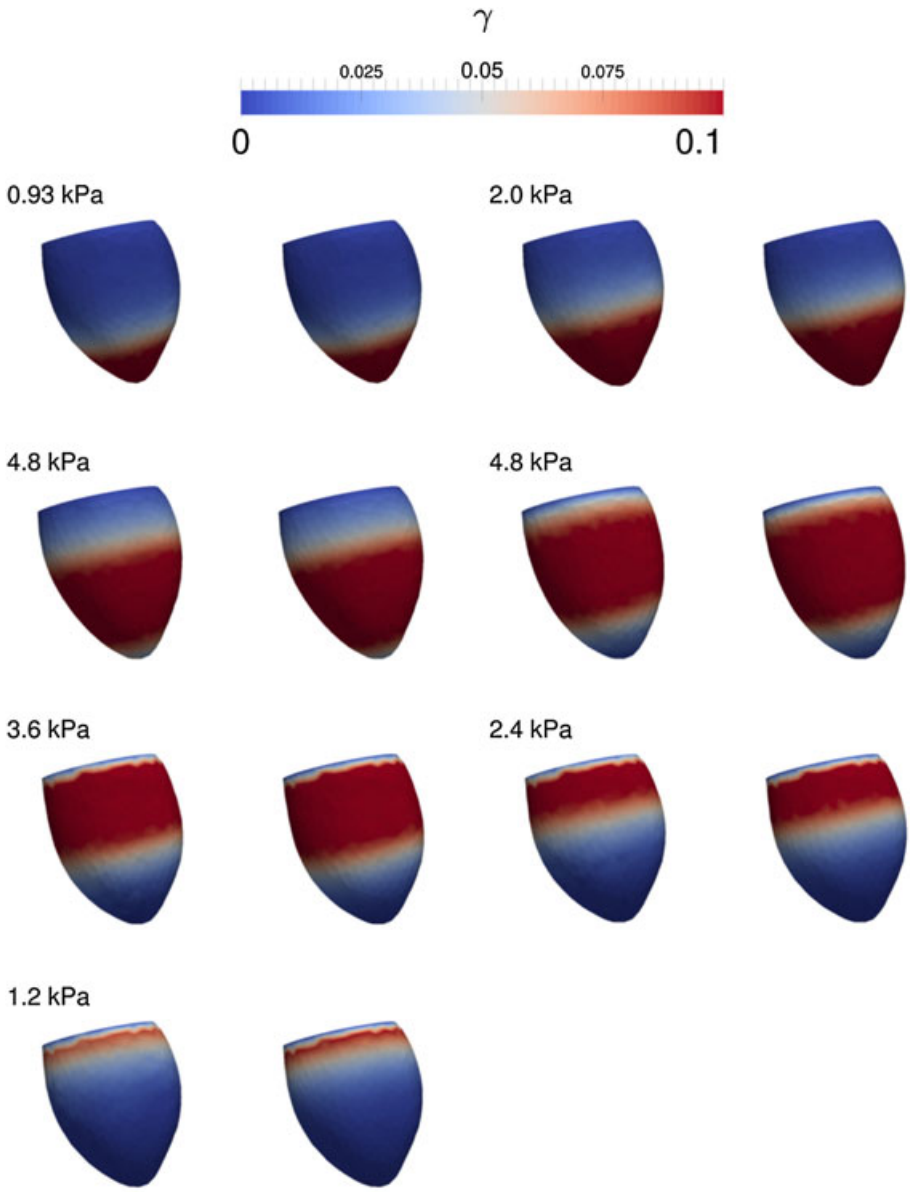

FIGURE 4 Lateral view of the ground truth and reconstructed contraction fields at 7 measurement points during the synthetic data test. The target for the optimization is the full strain field with no noise. At each pressure the reconstruction is displayed on the left and the ground truth on the right

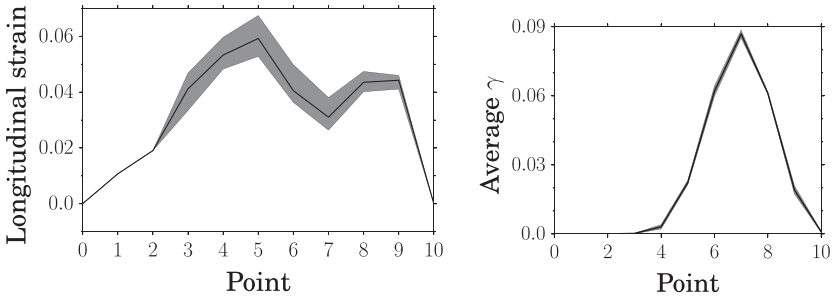

FIGURE 5 On the left are the mean (solid line) and standard deviation (highlighted area) of 30 synthetic longitudinal strain curves in the anterior basal segment corrupted by Gaussian noise. On the right are the mean and standard deviations of γ estimated averaged over the same segment

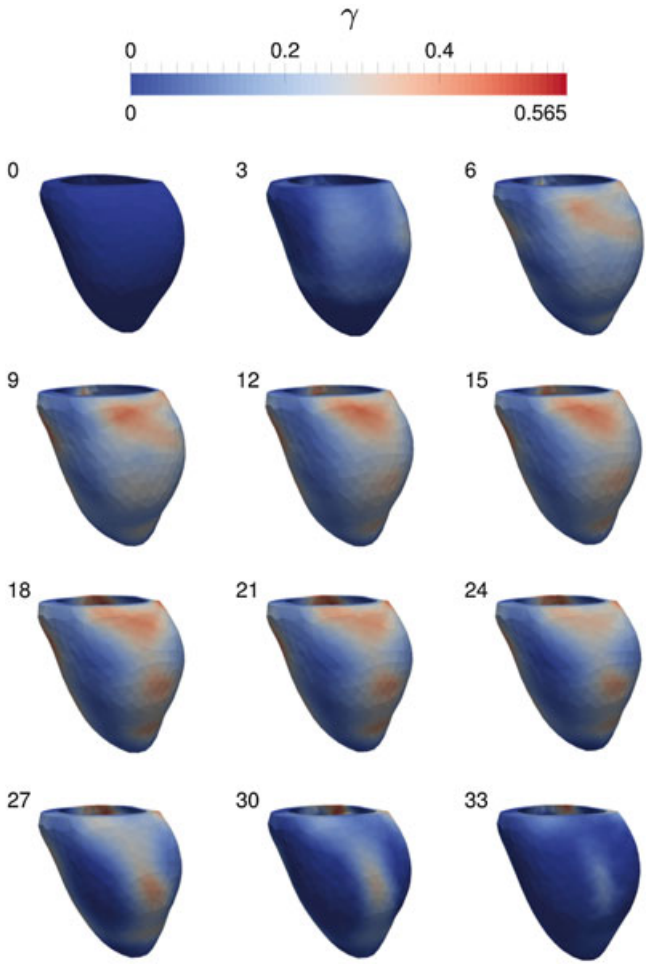

FIGURE 6 Posterior view of the contraction field γ optimized to in vivo data at P1 resolution. A snapshot is shown for every third in vivo measurement point

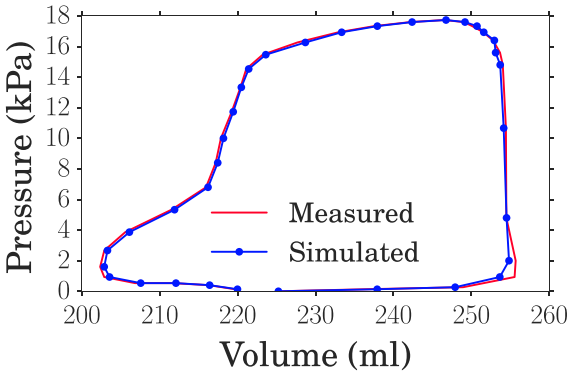

FIGURE 7 Clinically measured (red) versus optimized wall motion model (blue) left ventricular cavity volumes

3.5 | Contraction estimation with in vivo data

Using the in vivo data described in Section 2.2 as a target, we calculated optimized contraction fields at P1 resolution. These contraction fields are shown in Figure 6. We note that the value of the contraction varies significantly in space and time. A comparison of the estimated to the measured pressure - volume (PV) loop is shown in Figure 7. Optimized and measured strains are compared in Figure 8.

3.6 | Effect of contraction parameter resolution

To quantify the effects of the resolution of the contraction field γ, we have repeated the contraction estimation from in vivo data using regional and scalar resolutions. The fit values obtained for these resolutions are compared with the fit value of the P1 resolution in Table 2. The results show that the P1 resolution of γ gives an order of magnitude better strain and volume matches than the scalar and regional resolutions, and that $\bar{I}_{\text{strain}}^{\text{relmax}}$ is about an order of magnitude lower than $\bar{I}_{\text{strain}}$ in all 3 cases.

The computational cost of the data assimilation using the 3 resolutions of γ is compared in Table 1. We note that the number of forward and adjoint solves increases with the resolution and that the average run time of an adjoint solve in the scalar and P1 resolutions are almost the same.

4 | DISCUSSION

In our study, we have created a personalized model of whole cycle ventricular mechanics based on strain, volume, and pressure measurements of a dyssynchronous LV. The contraction parameter in our study was resolved at a high P1 level of resolution. Previous studies[8,11] have considered contraction parameters that were resolved up to the regional level of AHA zones. By comparing our P1 results to those generated with a regional resolution, we have shown that it is

TABLE 1 Performance of the contraction optimization with the clinical data for different resolutions of contraction parameter γ. The second and third column display the average number of forward and adjoint solves required to optimize γ at a single measurement point. The fourth column shows the total run time over all measurement points and the final column the average run time of an adjoint solve

Resolution of γ	Forward solves Average	Adjoint solves Average	Total run time (s)	Adjoint evaluation Average run time (s)
Scalar	4.6	2.8	280	7.4
Regional	12	6.5	210	19.3
P1	46	46	1100	7.9

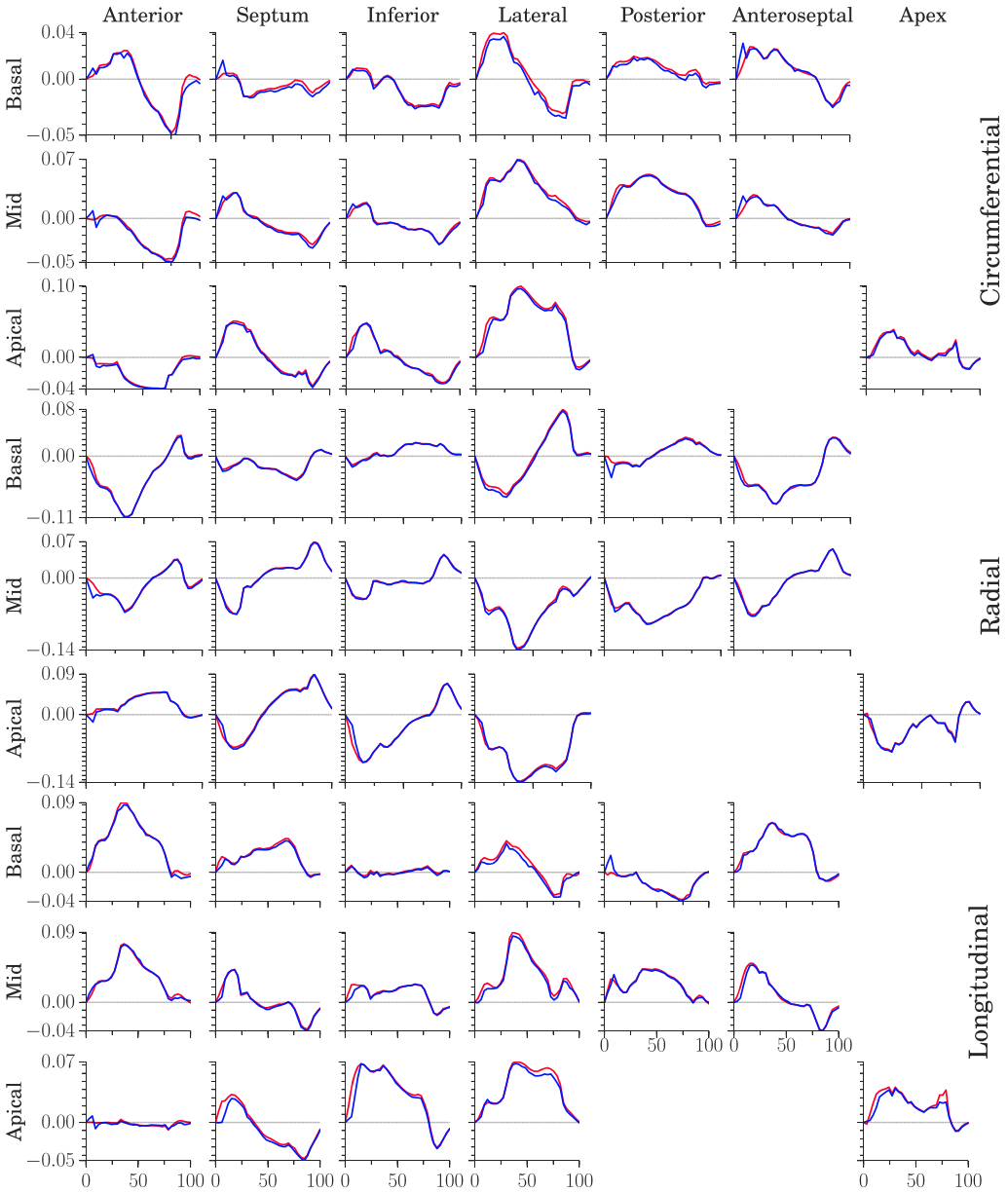

FIGURE 8 Comparison of regional strain curves starting in end diastole. In red: optimized wall motion model data. In blue: clinical data from speckle tracking echocardiography. In each plot, the *y*-axis represents strain while the *x*-axis shows the progression in time of the cardiac cycle as a percentage

possible to greatly increase the fitting ability of a data assimilation method by increasing the parameter resolution. Indeed, Table 2 shows that the fits $\bar{I}_{\text{vol}}$, $\bar{I}_{\text{strain}}$, and $\bar{I}_{\text{strain}}^{\text{relmax}}$ are an order of magnitude better for the P1 resolution as compared to the regional or scalar resolutions.

Errors in strain fitting were significant at the P1 resolution when compared to the sizes of the strain curves ($\bar{I}_{\text{strain}} = 0.17$). These errors can stem from a fundamental model-data mismatch, and or an inability of the data assimilation to fit the model to the data. In the case of a model-data mismatch,

TABLE 2 Relative misfit for different representation of γ

Resolution of γ	$\bar{I}_{\text{vol}}$	$\bar{I}_{\text{strain}}$	$\bar{I}_{\text{strain}}^{\text{relmax}}$
Scalar	0.044	1.5	0.27
Regional	0.024	1.1	0.16
P1	0.0037	0.17	0.029

the limitations of the model may play a role (see Section 4.1). Another cause of model-data mismatch is inaccuracy or noise in measurements, in which case, the model can be used to improve the measurements. This is the case when models are used to regularize image-based motion.[37,38]

The SQP optimization algorithm that we used is a local search only, so that is possible that our fitting was suboptimal, possibly contributing to the mismatch in strain. Adding regularization has been shown to prevent such suboptimal results in fluid control problems [[39] page 123]. This partially motivated our use of regularization in the contraction optimization (Equation 17).

The discrepancies between our model-based and measured strains are very small, however, when compared to the sizes of the largest strain curves of a given strain type, longitudinal, circumferential, or radial. This can clearly be seen in Figure 8 and in the low value of the metric $\bar{I}_{\text{strain}}^{\text{relmax}}$. This shows that our method was able to accurately capture the larger amplitude features of the heterogeneity in contraction. Such features are less prone to distortion by noise then those with smaller strain values and are therefore more relevant for potential medical use. However, the question of how much model resolution is actually needed to provide medically useful information remains an open one.

As a consequence of increased dimensionality in the optimization, estimating the contraction γ took just under 4 times longer with the P1 resolution than the scalar resolution. This was due to an increase in the number of forward and adjoint evaluations needed at the higher resolution. However, the average run time of an adjoint gradient evaluation did not differ significantly in the P1 case. This near invariance of the gradient calculation cost to the number of optimization parameters is an advantage of the adjoint-gradient method. In the case of the regional resolution, the average adjoint-gradient run time was nearly double that of the other 2 cases. This was due to increased symbolic computation required by the software dolfin-adjoint to differentiate characteristic functions defined over each AHA segment. The total run time for the scalar case was higher than for the regional case, despite the scalar case requiring fewer forward and adjoint evaluations. This was due to a greater number of Newton iterations required per forward solve in the scalar case.

To test the effects of mesh resolution on the contraction estimation, we have considered alternative mesh resolutions in Appendix C. The analysis shows that the tested increase and decrease in the resolution of the mesh did not significantly change the fit quality of the contraction estimation (Table C1). There were, however, slight differences in the spatial average of the contraction field between the 3 cases tested (Figure C1). This was most likely due to differences in the quality of the discrete approximation of the work balance equation (2).

In the current study, the resolution of the computational mesh affected both the resolution of the contraction field and the resolution of the displacement-pressure variables in the finite element model. The results of the mesh resolution tests suggest our contraction field may have been too highly resolved and that it might be beneficial to select the resolution of the contraction variable independently of the mesh in future studies. This would require specifying a set of basis functions for γ, which could be designed to allow for a good fit of model to data while at the same time minimizing the number of degrees of freedom. Such a procedure has been previously implemented for parameter estimation in groundwater modelling.[40]

To test the accuracy of the contraction estimation, we have conducted synthetic data tests for which the true contraction field was known. The results of these tests show that our data assimilation is greatly effected by the sparsity of data. Indeed, the approximation of γ was an order of magnitude better with strains that had all 6 components and were defined everywhere on the geometry, as compared to the regionally averaged strains limited to the tensor diagonal. This result did not hold at the apex where the maximum errors were the same for all 3 cases.

The regionally averaged strain representation is easier for a human to interpret and is widely used in medical research. However, for the purposes of building accurate personalized models, more resolution of strain is highly advantageous. The synthetic tests also showed that our data assimilation is not greatly effected by noise in the echocardiographic measurements. This is most likely due to our use of regularization, which favoured smoother solutions that averaged out the effects of the noise.

In addition to noise in strain, we can also expect inaccuracies in volume measurements from echocardiography. This is an issue for the estimation of the elastic parameter a, which we conducted purely from volume measurements. Experiments with gel phantoms have quantified this inaccuracy for assessments of a single image.[41] However, for the estimation of the elastic parameter a, relative differences in errors between images are more relevant. These have to the best of our knowledge not been studied and so we have conducted estimations of a with volume curves perturbed by a range of errors (see Appendix 3.1). These experiments show that the estimated stiffness parameter is indeed sensitive to volume errors. The effect on the average of the contraction field is, however, quite minimal. An alternative to the current stiffness estimation procedure would be to allow for greater spatial resolution from strain measurements as per the contraction parameter. This might allow for a regularized stiffness field to average out the effects of noisy measurements.

The volume fit between model and data was close for the 3 points in atrial systole, but differed in early isovolumic contraction. Indeed, the model underestimated the measured volumes, indicating an overestimation of ventricular stiffness at these points. This is a consequence of fitting the stiffness parameters to the atrial systolic points, and not to the points in early isovolumic contraction afterwards. If the effects of contraction could be isolated from the effects of elasticity, it would be possible to include these points in the elastic parameter fitting and possibly obtain a better match of volumes.

In our study, we personalized only a single elastic parameter a, which was done for the sake of simplicity. Previous studies have successfully estimated greater numbers of elastic parameters for the reduced Holzapfel law[9] and the fully orthortropic Holzapfel law.[3] Such procedures could be potentially combined with our contraction estimation to increase the level of model personalization. Another potential improvement of the elastic parameter estimation we used is the inclusion of aggregated geometry measures, such as short axis and long axis diameters. Such measures have been shown to improve identifiability of elastic parameters in experiments with mouse ventricles.[42]

Several data assimilation studies[5,6] have included objective functionals consisting of strain and volume components with equal weighing given to both. We have shown that it may be possible to improve such data assimilation procedures by tuning the relative weight of strain and volume components. Indeed, in the top right plot of Figure 3, there is a definite corner in the strain-volume fitting space consisting of 4 points beneath $\alpha = 0.95$. Choosing α among these points gives a fair trade-off between strain and volume matching whereas any choice outside this corner simply worsens the fit of strain or volume without much improving the other.

In Figure 3, we have shown how the parameters α and λ affect the fitting and smoothness metrics related to the contraction field γ. Additionally, we have tested the effects of variations in α and λ on the spatial average of the contraction field. These experiments are presented in Appendix D. Figure D1 shows that varying α in the region [0, 0.5] had little to no effect on the spatial average of γ, whereas increases in α outside of this region tended to increase the amount of contraction. This behaviour correlates with the value of $\bar{I}_{\text{strain}}$ in (Figure 3 top right). Similarly, increasing λ beyond 0.001 tended to increase the misfit in the data functional (Figure 3 bottom right) and also increase the average amount of contraction (Figure D1 right). We hypothesize that additional levels of misfit in strain introduced by increasing α beyond 0.5 and or λ beyond 0.001 lead to overestimating the amount of contraction in our patient's LV. However, we lack knowledge of the true amount of muscle contraction in the patient, which could be used to test the hypothesis. Further validation of the model and data assimilation are needed.

4.1 | Limitations

The results obtained in this article were limited by issues pertaining to the choice of mathematical model, quality of clinical data, numerical stability, and the design of the data assimilation algorithm. Firstly, the boundary conditions of the ventricle wall motion model did not account for the effects of the right ventricular pressure on the septum and the mechanical coupling to the neighboring structures: left atrium, right ventricle, and pericardium.

The in vivo circumferential and radial motion at the base was not incorporated into the model. Instead, some motion was allowed by the basal spring, whose constant k needed to be chosen. In the future, we would like to incorporate basal motion data from the images into our personalized model. This would allow us to avoid having to make a choice of k and hopefully allow for the reproduction of in vivo basal motion in the personalized model.

During the atrial systole phase, we assumed $\gamma = 0$. This allowed for the estimation of passive properties separate from contraction. This assumption is appropriate for a healthy ventricle but might be false in a diseased ventricle if muscle relaxation is sufficiently delayed.

Our mathematical model of wall motion neglected the effects of viscoelasticity, tissue compressibility,[43] inertia, and myocardial sheet microstructure. Finally, the reference geometry that we used for our calculations came from an echocardiographic image in which there was a nonzero level of blood pressure. The blood pressures we used in our patient specific model were off by the 2.8 kPa that we subtracted to have 0 pressure in the reference geometry. This pressure adjustment meant that the elastic stiffness of the ventricle was underestimated by our elastic parameter estimation, as the mathematical model operated at a lower pressure than measured in the patient's heart.

The accuracy of the optimized motion model was limited by uncertainties in the clinical strain and volume measurements, which were related to echocardiographic image quality, image sample rate, and speckle tracking algorithm accuracy. Pressure and volume measurements had to be synchronized, which might have lead to a potentially unphysiological loss of volume in the iso-volumic relaxation phase of the in vivo PV loop (Figure 1).

Finally, there were several algorithmic limitations. Firstly, the optimized γ fields we computed may or may not have been unique. For potential clinical applications, this is a concern as the uniqueness of parameters relate to the reproducibility and consistency of data obtained from a personalized model. Furthermore, our procedures for choosing the functional weights α and λ were not optimal. In both the synthetic and clinical data case, the weight values were chosen by parameter sweeps that kept a single parameter fixed, which did not account for possibly better α,λ combinations lying outside of the areas we tested. Finally, the SQP optimization algorithm that we used was a local search only, that is, only one minimum of the objective is calculated. Better parameter fits may be pos-

sible with global optimization methods that explore multiple minima.

5 | CONCLUSION AND FUTURE OUTLOOK

By using high-resolution data assimilation, we were able to capture the detailed motion of a dyssynchronous LV in a computational model with an excellent fit of model observations to data. This demonstrates the power of the data assimilation method, which can also be applied to other models and or model parameters.

In the future, the proposed method should be further improved and tested on cohorts of patients. This would allow for the study of simulated contraction patterns among groups of patients that could lead to further understanding of dyssynchrony.

6 | AUTHOR DECLARATION

All of the clinical data for this study was collected with the approval of the Norwegian national ethics committee, REC, and in accordance to the Helsinki Declaration of 1975, as revised in 2000.

ACKNOWLEDGMENTS

Computations were performed on the Abel supercomputing cluster at the University of Oslo via Notur projects nn9316k and nn9249k.

Funding was provided by the Research Council of Norway via the Center for Biomedical Computing at Simula Research Laboratory (grant 179578), and via the Center for Cardiological Innovation at Oslo University Hospital (grant 203489).

REFERENCES

1. Sermesant M, Moireau P, Camara O, et al. Cardiac function estimation from MRI using a heart model and data assimilation: Advances and difficulties. *Med Image Anal*. 2006;10(4):642–656.
2. Augenstein KF, Cowan BR, LeGrice IJ, Nielsen PM, Young AA. Method and apparatus for soft tissue material parameter estimation using tissue tagged magnetic resonance imaging. *J Biomech Eng*. 2005;127(1):148–157.
3. Gao H, Li WG, Cai L, Berry C, Luo X. Parameter estimation in a Holzapfel–Ogden law for healthy myocardium. *J Eng Math*. 2015;95(1):231–248.
4. Wang VY, Lam HI, Ennis DB, et al. Modelling passive diastolic mechanics with quantitative MRI of cardiac structure and function. *Med Image Anal*. 2009;13(5):773–84.
5. Mojsejenko D, McGarvey JR, Dorsey SM, et al. Estimating passive mechanical properties in a myocardial infarction using MRI and finite element simulations. *Biomech Model Mechanobiol*. 2014;14(3):633–647.
6. Sun K, Stander N, Jhun CS, et al. A computationally efficient formal optimization of regional myocardial contractility in a sheep with left ventricular aneurysm. *J Biomech Eng*. 2009;131(11):111001–111001-10.
7. Neumann D, Mansi T, Georgescu B, et al. Robust image-based estimation of cardiac tissue parameters and their uncertainty from noisy data, *Medical Image Computing and Computer-Assisted Intervention–MICCAI 2014*. New York, NY: Springer; 2014:9–16.
8. Wong KC, Sermesant M, Rhode K, et al. Velocity-based cardiac contractility personalization from images using derivative-free optimization. *J Mech Behav Biomed Mater*. 2015;43:35–52.
9. Asner L, Hadjicharalambous M, Chabiniok R, et al. Estimation of passive and active properties in the human heart using 3d tagged mri. *Biomech Model Mechanobiol*. 2015:1–19.
10. Hadjicharalambous M, Chabiniok R, Asner L, et al. Analysis of passive cardiac constitutive laws for parameter estimation using 3D tagged MRI. *Biomech Model in Mechanobiol*. 2015;14(4):807–828.
11. Chabiniok R, Moireau P, Lesault P-F, et al. Estimation of tissue contractility from cardiac cine-MRI using a biomechanical heart model. *Biomechanics and Model in Mechanobiol*. 2012;11(5):609–630.
12. Xi J, Lamata P, Lee J, et al. Myocardial transversely isotropic material parameter estimation from in-silico measurements based on a reduced-order unscented Kalman filter. *J Mech Behav Biomed Mater*. 2011;4(7):1090–1102.
13. Marchesseau S, Delingette H, Sermesant M, et al. Preliminary specificity study of the Bestel-Clément-Sorine electromechanical model of the heart using parameter calibration from medical images.*J Mech Behav Biomed Mater*. 2013;20:259–71.
14. Delingette H, Billet F, Wong KCL, et al. Personalization of cardiac motion and contractility from images using variational data assimilation. *IEEE Trans Biomed Eng*. 2012;59(1):20–24.
15. Sundar H, Davatzikos C, Biros G. Biomechanically-constrained 4D estimation of myocardial motion. *Medical Image Computing and Computer-Assisted Intervention–MICCAI, London, UK, 2009*. New York, NY: Springer; 2009:257–265.
16. Balaban G, Alnæs MS, Sundnes J, Rognes ME. Adjoint multi-start-based estimation of cardiac hyperelastic material parameters using shear data. *Biomech Model Mechanobiol*. 2016;15(6):1–13.
17. Krishnamurthy A, Villongco CT, Chuang J, et al. Patient-specific models of cardiac biomechanics. *J Comput Phys*. 2013;244:4–21.
18. Gjerald S, Hake J, Pezzuto S, Sundnes J, Wall ST. Patient–specific parameter estimation for a transversely isotropic active strain model of left ventricular mechanics. *Statistical Atlases and Computational Models of the Heart-Imaging and Modelling Challenges*. New York, NY: Springer; 2015:93–104.
19. Holzapfel Ga, Ogden RW. Constitutive modelling of passive myocardium: a structurally based framework for material characterization. *Philos Trans Ser A Math Phys Eng Sci*. 2009;367(1902):3445–75.
20. Land S, Niederer S, Lamata P, et al. Improving the stability of cardiac mechanical simulations. *IEEE Trans Biomed Eng*. 2015;62(3):939–947.
21. Nardinocchi P, Teresi L. On the active response of soft living tissues. *J Elast*. 2007;88(1):27–39.
22. Evangelista A, Nardinocchi P, Puddu PE, et al. Torsion of the human left ventricle: experimental analysis and computational modeling. *Prog Biophys Mol Biol*. 2011;107(1):112–121.
23. Hospital OU. Acute feedback on left ventricular lead implantation location for cardiac resynchronization therapy (CCI impact). 2016. https://clinicaltrials.gov. Accessed September 1, 2016.
24. Cerqueira MD, Weissman NJ, Dilsizian V, et al. Standardized myocardial segmentation and nomenclature for tomographic imaging of the heart a statement for healthcare professionals from the cardiac imaging committee of the Council on Clinical Cardiology of the American Heart Association. *Circulation*. 2002;105(4):539–542.
25. Bols J, Degroote J, Trachet B, et al. A computational method to assess the in vivo stresses and unloaded configuration of patient-specific blood vessels. *J Comput Appl Math*. 2013;246:10–17.
26. Gee MW, Förster C, Wall WA. A computational strategy for prestressing patient-specific biomechanical problems under finite deformation. *Int J Numer Meth Biomed Eng*. 2010;26(1):52–72.
27. Geuzaine C, Remacle JF. Gmsh: A 3-D finite element mesh generator with built-in pre-and post-processing facilities. *Int J Numer Meth Eng*. 2009;79(11):1309–1331.

28. Bayer JD, Blake RC, Plank G, Trayanova NA. A novel rule-based algorithm for assigning myocardial fiber orientation to computational heart models. *Annals of Biomed Eng*. 2012;40(10):2243–2254.
29. Hood P, Taylor C. Navier-stokes equations using mixed interpolation. *Finite Elem Meth Flow Prob*. 1974:121–132.
30. Logg A, Mardal KA, Wells GN, et al. *Automated Solution of Differential Equations by the Finite Element Method*. New York, NY: Springer; 2011.
31. Balay S, Brown J, Buschelman K, et al. PETSc web page. 2015. http://www.mcs.anl.gov/petsc. Accessed September 1, 2016.
32. Li XS, Demmel JW. SuperLUDIST: A scalable distributed-memory sparse direct solver for unsymmetric linear systems. *ACM Trans Math Softw*. 2003;29(2):110–140.
33. Kraft D. *A Software Package for Sequential Quadratic Programming*. Germany: DFVLR Obersfaffeuhofen; 1988.
34. Farrell PE, Ham DA, Funke SW, Rognes ME. Automated derivation of the adjoint of high-level transient finite element programs. *SIAM J Sci Comput*. 2013;35(4):C369–C393.
35. Pezzuto S, Ambrosi D, Quarteroni A. An orthotropic active–strain model for the myocardium mechanics and its numerical approximation. *Eur J Mech-A/Solids*. 2014;48:83–96.
36. Finsberg H, Balaban G. High resolution data assimilation of cardiac mechanics. 2016. http://www.bitbucket.org/finsberg/cardiac_highres_dataassim. Accessed September 1, 2016.
37. Papademetris X, Sinusas AJ, Dione DP, Constable RT, Duncan JS. Estimation of 3-d left ventricular deformation from medical images using biomechanical models. *IEEE Trans Med Imaging*. 2002;21(7):786–800.
38. Tuyisenge V, Sarry L, Corpetti T, et al. Estimation of myocardial strain and contraction phase from cine mri using variational data assimilation. *IEEE Trans Med Imaging*. 2016;35(2):442–455.
39. Gunzburger MD. *Perspectives in Flow Control and Optimization*. Philadelphia: Siam; 2002.
40. Tsai FTC, Sun NZ, Yeh WWG. Global-local optimization for parameter structure identification in three-dimensional groundwater modeling. *Water Resour Res*. 2003;39(2):1043.
41. Aurich M, André F, Keller M, et al. Assessment of left ventricular volumes with echocardiography and cardiac magnetic resonance imaging: real-life evaluation of standard versus new semiautomatic methods. *J Am Soc Echocardiography*. 2014;27(10):1017–1024.
42. Nordbø Ø, Lamata P, Land S, et al. A computational pipeline for quantification of mouse myocardial stiffness parameters. *Comput Biol Med*. 2014;53:65–75.
43. Yin F, Chan C, Judd RM. Compressibility of perfused passive myocardium. *Am J Physiol-Heart Circulatory Physiol*. 1996;271(5):H1864–H1870.

How to cite this article: Balaban G, Finsberg H, Odland HH, Rognes ME, Ross S, Sundnes J, Wall S. High-resolution data assimilation of cardiac mechanics applied to a dyssynchronous ventricle. *Int J Numer Meth Biomed Engng*. 2017;33:e2863. https://doi.org/10.1002/cnm.2863

APPENDIX A

SENSITIVITY OF ELASTIC PARAMETER TO ERROR IN ATRIAL SYSTOLIC VOLUME MEASUREMENTS

To test the sensitivity of our estimated a parameter to uncertainty in volume measurements, we have conducted a series of estimations with various levels of volume perturbation.

TABLE A1 Sensitivity of the optimized material parameter a to errors in volume measurements. The first column gives the perturbation of the volume increase between measurement points 1-2 and 2-3, in percent. The next 2 columns give the size of these perturbations in milliliters with ΔV_2 and ΔV_3 referring to perturbations in the volumes of the second and third measurement points, respectively. In the fourth column, optimal a values are given. In all cases, the volume fit $\bar{I}_{\text{vol}}$ was less than 4×10^{-6}

Perturbation (%)	ΔV_2 (ml)	ΔV_3 (ml)	a (kPa)
−25	−1.2	−1.06	0.494
−15	−0.717	−0.636	0.469
−5	−0.239	−0.212	0.446
0	0	0	0.435
5	0.239	0.212	0.424
15	0.717	0.636	0.404
25	1.2	1.06	0.384

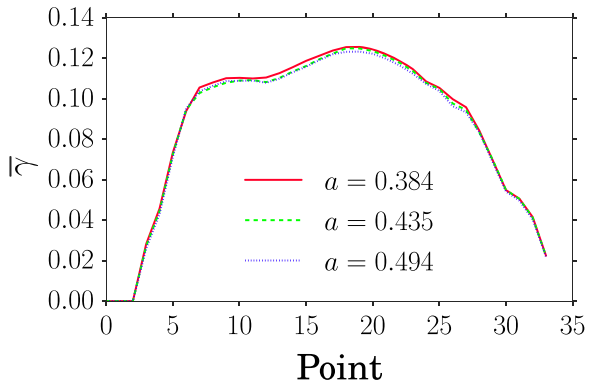

FIGURE A1 Sensitivity of the optimal average contraction $\bar{\gamma}$ to changes in the parameter a. The upper and lower a values are based on estimating a with volume perturbations of ± 25% (Table A1). The middle value was obtained by estimating a from in vivo volumes

We generated clean volume data using the computational model using $a = 0.435$ kPa, the optimal value obtained from the clinical data. Perturbations in volume increases of sizes ± 5,15,25% were added to this data, which were then used as target for optimization. The resulting a values and perturbations are shown in Table A1. The largest perturbations resulted in the a values 0.494 kPa and 0.384 kPa, representing circa ± %13 change from the original a value.

The resulting average value of γ is shown in Figure A1 for the extreme cases with $\alpha = 0.494$ and $\alpha = 0.384$. For reference, we also include the average value of γ using $\alpha = 0.435$.

APPENDIX B

SENSITIVITY OF ESTIMATED PARAMETERS TO SPRING CONSTANT

The spring boundary condition that we used at the ventricular base has a significant effect on the simulated cavity volumes calculated by the model. This is due to the

TABLE B1 Sensitivity of optimal a value to choice of spring constant k

k	10^{-8}	10^{-7}	10^{-6}	10^{-5}	10^{-4}	10^{-3}	0.01	0.1	1	10	100	∞
a	0.875	0.875	0.875	0.875	0.873	0.873	0.849	0.684	0.435	0.375	0.366	0.365

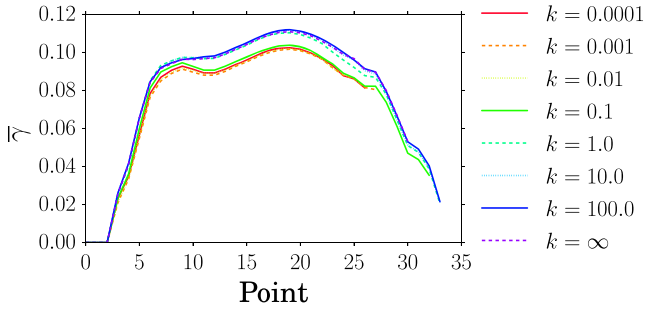

FIGURE B1 Sensitivity of the spatially averaged contraction $\bar{\gamma}$ to the choice of spring constant k

cross-sectional area of the cavity being large at the ventricular base. Therefore, we can expect the choice of k to have an effect on the optimal parameters calculated by our data assimilation.

To quantify this effect, we have conducted a sensitivity analysis, starting with the effect of k on the optimized elastic parameter a. We repeated the elastic parameter fitting decribed in Section 3.1 and varied the k-value from 0.001 to 100.0. We also considered the case $k = \infty$, denoting a completely rigid boundary held by Dirichlet boundary conditions. The effect of the choice of k on the optimal value of a is shown in Table B1. The table shows that the optimal a varies from 0.365 kPa to 0.875 kPa depending upon how the k parameter is set.

We also tested the sensitivity of the contraction γ at P1 resolution to k by repeating the estimation of γ with the various k and a pairs obtained in the previous experiment. For each k, a pair, we have plotted the spatial average of contraction $\bar{\gamma}$ at each measurement point in Figure B1. The results show up to a 20% variation in $\bar{\gamma}$ and very little variation for the choices of k greater than or equal to 1.0. For some of the values of $k < 1.0$, our homotopy Newton solver was unable to secure convergence during the optimization. Curves corresponding to these cases are drawn only to the point before the nonconvergence occurred.

APPENDIX C

EFFECT OF MESH RESOLUTION ON ESTIMATED CONTRACTION AT P1 RESOLUTION

Ventricular meshes were generated by Gmsh[27] with 3 different resolutions controlled by the parameter "Mesh.CharacteristicLengthFactor." This parameter was given the values 1.0, 0.65, and 0.45, which resulted in meshes with 549, 1262, and 2261 vertices, respectively. Using the 3 meshes, we estimated contraction fields from the in vivo data. The average value of γ is shown for these 3 cases in Figure C1. Fit quality is compared in Table C1.

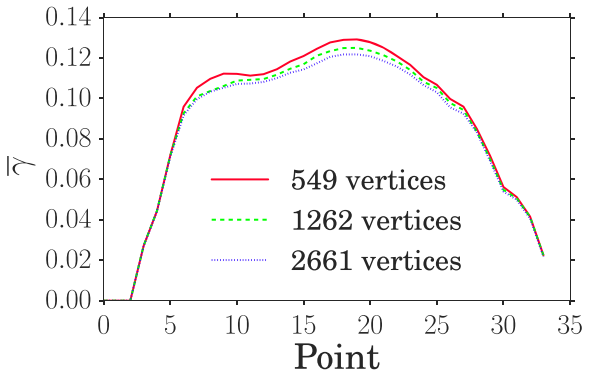

FIGURE C1 Spatial average of contraction $\bar{\gamma}$ for 3 different mesh resolutions

TABLE C1 Relative misfit for different mesh resolutions

Number of elements	$\bar{I}_{vol}$	$\bar{I}_{strain}$	$\bar{I}^{relmax}_{strain}$
549	0.0033	0.17	0.029
1262	0.0037	0.17	0.029
2661	0.0043	0.18	0.031

APPENDIX D

SENSITIVITY OF CONTRACTION SIZE TO CHOICES OF AND λ

On the basis of the trade-off curves in Figure 3, we chose the optimization weights $\alpha = 0.95$ and $\lambda = 0.01$ for the personalization of our wall motion model to the in vivo data. To show the effect of these choices on the optimized contraction field γ, we have varied the α and λ values and plotted the spatial averages of the resulting contraction fields. The results show that the amount of contraction tends to increase proportionally to both α and λ beyond the thresholds $\alpha = 0.5$ and $\lambda = 0.001$.

APPENDIX E

ESTIMATION OF NOISE IN ECHO SPECKLE TRACKING STRAIN MEASUREMENTS

To increase the relevance of the synthetic tests, we considered a set of regional strains that contained noise. This noise was modelled as an additive Gaussian process to imitate the

TABLE E1 Mean and covariance of a Gaussian noise summand estimated from patient drift values in circumferential (C), radial (R), and longitudinal (L) directions

	Covariance $\times 10^{-4}$ C	R	L	Mean
C	1.43	0.73	0.66	0.006
R	-	6.8	6.31	−0.013
L	-	-	7.26	0.01

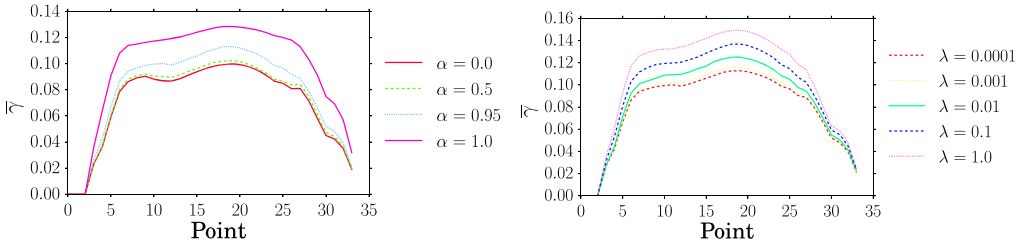

FIGURE D1 Sensitivity of the spatially averaged contraction $\overline{\gamma}$ to variations in optimization weights α and λ. Left: $\lambda = 0$ and α is varied. Right: $\alpha = 0.95$ and λ is varied

accumulation of tracking errors in EchoPac's image-based strain calculations. The mean and variance of a summand in the Gaussian process were estimated from our in vivo strain data of a single patient. From these data, the sample means and variances of the drift values were divided by the number of measurement points to approximate the noise in a single measurement. The mean and covariance of this single measurement point noise are given in Table E1. Theoretically, error-free strain curves would have no drift given stable conditions in the heart. This motivates the use of the drift values in order to approximate the tracking error.